Quantitative Role of Phonons and Elasticity in Tuning Uniaxial Negative Thermal Expansion of MZr_2 (M = Fe, Co, and Ni)

Meng Xu,[1] Qilong Gao,[2,†] Yongqiang Qiao,[2] Kaiyue Zhao,[2] Andrea Sanson,[3,4] Qiang Sun,[2] Changtian Wang,[1] Alessandro Venier,[3] Francesco d'Acapito,[5] Matt Tucker,[6] Yuzhu Song,[1] Chang Zhou,[1,7,‡] Xianran Xing,[8] and Jun Chen[1,9,*]

[1]*Department of Physical Chemistry, Beijing Advanced Innovation Center for Materials Genome Engineering, University of Science and Technology Beijing, Beijing 100083, China*
[2]*Key Laboratory of Materials Physics, Ministry of Education, School of Physics, Zhengzhou University, Zhengzhou 450001, China*
[3]*Department of Physics and Astronomy, University of Padua, Padova I-35131, Italy*
[4]*Department of Management and Engineering, University of Padua, Padova I-35131, Italy*
[5]*CNR-IOM-OGG, c/o ESRF, Grenoble F-38043, France*
[6]*Neutron Scattering Division, Oak Ridge National Laboratory, Oak Ridge, Tennessee 37831, USA*
[7]*State Key Laboratory for Advanced Metals and Materials, University of Science and Technology Beijing, Beijing 100083, China*
[8]*Institute of Solid State Chemistry, University of Science and Technology Beijing, Beijing 100083, China*
[9]*State Key Laboratory of Tropic Ocean Engineering Materials and Materials Evaluation, Hainan University, Haikou 570228, China*

(Received 20 August 2024; revised 10 March 2025; accepted 11 September 2025; published 15 October 2025)

Elucidating the mechanisms of negative thermal expansion (NTE) not only identifies the determining factors of this phenomenon but also provides guidance for the precise regulation of the coefficient of thermal expansion (CTE). However, accurately quantifying these determining factors during CTE modulation remains a critical challenge. In this Letter, we quantitatively determine the respective contributions of phonon-derived Grüneisen parameters (axial values and their difference) and elastic compliance tensors to the tuning of axial NTE in the MZr_2 system. Through temperature dependence of the neutron total scattering data (for neutron powder diffraction and neutron pair distribution function analyses), extended x-ray absorption fine structure, synchrotron x-ray diffraction, and first-principles calculations, it provides insight into the quantified roles of phonons and anisotropic elasticity in controlling the broad-range CTE. As the number of M-3d electrons grows, phonons, which are the dominant factors, weaken NTE, while elasticity, playing a cross-linking coefficient, enhances NTE. The current study not only provides deep insights into the origins of NTE in the MZr_2 system, but it also offers a novel perspective on the quantifiable control of NTE in anisotropic materials.

DOI: 10.1103/35ff-84fc

Introduction—Negative thermal expansion (NTE) materials demonstrate a distinctive physical attribute, whose dimensions contract as the temperature increases. NTE materials have been widely applied as thermal compensatory materials for positive thermal expansion (PTE) materials to enhance material stability and performance [1–5]. Over two decades of advancement, NTE phenomena have been detected in various material categories, such as cyanides [6,7], oxides [1,8], fluorides [9–11], metal-organic frameworks (MOFs) [12,13], and metallic materials [14,15]. The NTE is typically induced by two main mechanisms. The primary one is phonon driven, which is typically observed in framework materials like ZrW_2O_8 [1], ScF_3 [10], cyanides [6], and MOFs [13]. Another category encompasses electron driven, like spontaneous volume ferroelectrostriction in $PbTiO_3$ [16], magnetovolume effects in Invar alloys [17], and Mott transition in Ca_2RuO_4 [18]. Additionally, elasticity [19] and multiple effects [20,21] have also been employed to explain certain NTE phenomena.

A comprehensive understanding of NTE mechanisms provides valuable guidance for the development of regulation strategies. In isotropic framework materials, NTE is predominantly driven by phonons, as exemplified by classic examples such as ZrW_2O_8 [1,22], ScF_3 [10,11,23], and cyanides [24]. In anisotropic materials, NTE is determined not only by the anisotropy in phonons with negative mode Grüneisen parameters but also by anisotropic elasticity [25,26]. For instance, the anisotropic NTE of $A_2M_3O_{12}$ (M = W and Mo) materials is closely related to elastic anisotropy, where the NTE axis exhibits low compliance [27]. In uniaxial NTE Ruddlesden-Popper oxides, large off-diagonal elastic constant elements specific to the NTE phase are essential for enhancing NTE [26]. Despite differing views on the roles of phonons and elasticity in NTE, a comprehensive analysis and quantitative study of their

*Contact author: junchen@ustb.edu.cn
†Contact author: qilonggao@zzu.edu.cn
‡Contact author: changzhou@ustb.edu.cn

contributions to anisotropic thermal expansion, particularly elasticity, remain lacking. Therefore, quantifying the roles of phonons and elasticity in NTE helps to better understand their contributions to NTE and guides the regulation of thermal expansion, which is essential for the development of anisotropic NTE materials.

Currently, the tetragonal $CuAl_2$-type MZr_2 system (M = Fe, Co, and Ni) has been reported to exhibit fascinating broad temperature ranges with giant and strong NTE properties [28,29]. Here, we systematically investigated the thermal expansion behavior of the MZr_2 solid solution. For the first time in the MZr_2 system, the origin of NTE has been revealed through the quantified contributions between phonons and elasticity confirmed by experiments and first-principles calculations. Interestingly, the system exhibits a broadly adjustable coefficient of thermal expansion (CTE) from giant NTE, moderate NTE, zero thermal expansion (ZTE), to PTE. This pronounced CTE tunability mechanism has been uncovered through a comprehensive analysis that combines the temperature dependence of the neutron total scattering data [for the neutron pair distribution function (NPDF) and neutron powder diffraction (NPD) analyses], synchrotron x-ray diffraction (SXRD), extended x-ray absorption fine structure (EXAFS), and first-principles calculations. As the number of M-3d electrons grows, the phonon-dominated axial Grüneisen parameters ($\bar{\gamma}_a$ and $\bar{\gamma}_c$) and their difference ($\bar{\gamma}_c$-$\bar{\gamma}_a$) primarily govern the regulation of CTE, acting to weaken NTE. Meanwhile, elasticity-dominated compliance tensors serving as coefficients of the Grüneisen parameters enhance NTE. This Letter provides a novel approach for understanding the nature of thermal expansion, achieving broad-range CTE regulation, and guiding the discovery of new NTE materials.

Results—A series of MZr_2 solid solutions were prepared by arc melting. NPD and SXRD measurements confirmed that all samples possessed the same $CuAl_2$-type structure and crystallize with a $I4/mcm$ tetragonal lattice (see Supplemental Material Figs. S1 and S2 [30]). The crystal structure has two Wyckoff positions, with M and Zr atoms occupying the $4a$ (0, 0, 0.25) and $8h$ $(x, x+0.5, 0)$ positions, respectively [Fig. 1(a)].

The temperature dependence of NPD within the MZr_2 system was conducted to acquire detailed thermal expansion information. Interestingly, the thermal expansion behavior of the MZr_2 system exhibits continuous and systematic changes with an increasing number of M-3d electrons [Fig. 1(b)]. The lattice parameter of the c axis for $FeZr_2$ rapidly and smoothly decreases with increasing temperature, exhibiting giant NTE ($\alpha_c = -44.63 \times 10^{-6}$ K^{-1}, 150–500 K), consistent with our previous report [28]. As the M-3d electron count increases, $(Fe_{0.5}Ni_{0.5})Zr_2$ and $CoZr_2$ display moderate NTE along the c axis. The CTEs of α_c are -17.80×10^{-6} K^{-1} and -16.54×10^{-6} K^{-1}, respectively, and differ insignificantly in numerical terms. Further increasing the M-3d electron count results in near

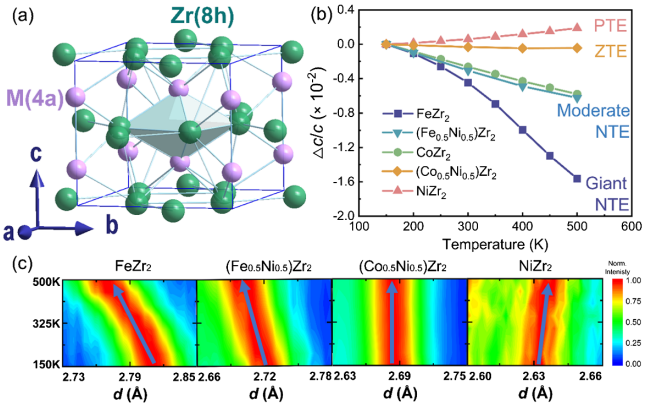

FIG. 1. (a) Crystal structure of MZr_2. (b) Temperature dependence of the $\Delta c/c$ for MZr_2. (c) Contour plot of the normalized (002) diffraction peak extracted from NPD patterns.

ZTE ($\alpha_c = -1.24 \times 10^{-6}$ K^{-1}) for $(Co_{0.5}Ni_{0.5})Zr_2$ along the c axis. The magnitude of CTE is very close to that of Invar alloy. The end point composition $NiZr_2$ exhibits normal PTE ($\alpha_c = 5.37 \times 10^{-6}$ K^{-1}).

The (002) diffraction peak of NPD demonstrates the broad adjustability of CTE across a wide temperature range. In $FeZr_2$, this peak rapidly shifts to lower d values with increasing temperature, while in $CoZr_2$, the shift decreases, remains stable in $(Co_{0.5}Ni_{0.5})Zr_2$, and reverses to higher d values in $NiZr_2$ [Fig. 1(c)]. This illustrates the continuous broad tuning of thermal expansion along the c axis from giant NTE to moderate NTE, ZTE, and finally PTE. Moreover, the temperature dependence of the lattice parameter a and unit cell volume (V) in the MZr_2 system shows that both exhibit PTE across all MZr_2 solid solutions (see Supplemental Material Figs. S3 and S4 [30]). Bulk XRD indicates a strong texture along the vertical direction (VD) of the ingot, with the [001] axis aligned parallel to the VD [Supplemental Material Fig. S5(a) [30]]. The strong VD texture of the ingots causes their thermal expansion to closely match the lattice parameter c of the same solid solution [Supplemental Material Fig. S5(b) [30]]. These solid solutions exhibit giant NTE and strong NTE. When combined with PTE materials to form structural devices in a one-dimensional (rodlike) direction, they can counteract the significant thermal expansion displacement of the PTE materials.

To illustrate how the atomic vibrational behavior with the lattice structure results in significant CTE regulation, the atomic displacement parameters (ADPs) of all solid solutions were extracted from NPD and NPDF (Supplemental Material Figs. S7 and S8 [30]). Anisotropic ADPs characterize the atomic vibrational dynamics in the crystal by describing the shape and direction of atomic displacement ellipsoids (assuming no static disorder) and can be expressed using Uij (i, j = 1, 2, or 3) [4,48,49]. In the MZr_2 system, Zr-U12 shows the most pronounced variation among all ADPs (Supplemental Material Figs. S7 and S8 [30]). The magnitude of Zr-U12 controls the extent

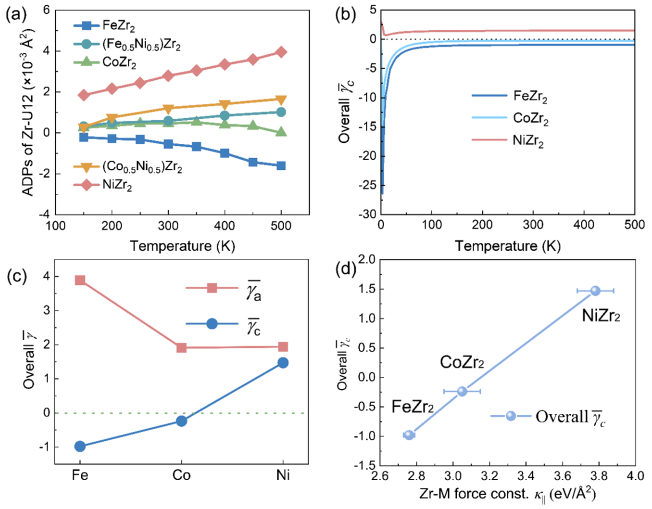

FIG. 2. (a) Temperature dependence of ADPs of the Zr-U12 for MZr_2 extracted from NPD. (b) Temperature dependence of the overall $\bar{\gamma}_c$ for $FeZr_2$, $CoZr_2$, and $NiZr_2$. (c) The overall $\bar{\gamma}_a$ and $\bar{\gamma}_c$ values at 300 K for $FeZr_2$, $CoZr_2$, and $NiZr_2$. (d) Relationship between the bond-stretching effective force constants ($\kappa_{||}$) of the $Zr-M$ bonds derived by EXAFS and the overall $\bar{\gamma}_c$ at 300 K. The values of $\kappa_{||}$ for $FeZr_2$ and $NiZr_2$ are taken from previous work [28].

of flattening in the ellipsoid's projection on the a-b plane (detailed in Supplemental Material Fig. S9 and its annotation [30]). It is observed that $FeZr_2$ shows a giant NTE with the most negative Zr-U12 [Fig. 2(a)]. With increasing M-3d electron count, both Zr-U12 and CTE rise monotonically, and in $NiZr_2$, both become positive. ADPs represent a statistical outcome of the superposition of all phonon vibrational modes [50,51], and the Grüneisen parameter is one of the factors influencing CTE [4,22]. The consistent trend between Zr-U12 and CTE suggests that both Zr-U12 and CTE are related to lattice dynamics. This simultaneously implies that the broad tunability of CTE in MZr_2 is intrinsically connected with atomic vibration characteristics.

Phonon dispersion curves offer profound insights into atomic vibration characteristics. To quantify the role of phonons in regulating CTE, the phonon spectra of three end point compositions $FeZr_2$, $CoZr_2$, and $NiZr_2$ have been computed. With an increase in M-3d electrons, the number of vibrational modes generating negative Grüneisen parameters along the c axis (γ_c) remarkably decreases (Supplemental Material Fig. S10 [30]). Typically, the magnitude of the γ value represents the extent of contribution to thermal expansion [9,52]. In the MZr_2 system, the negative γ_c excited by phonon vibrational modes acts as a thermal driver, signifying a contribution to NTE along the c axis. $FeZr_2$ exhibits the highest number of negative γ_c vibrational modes among the three end point compositions, corresponding to a giant uniaxial NTE. The number of negative γ_c vibration modes in $CoZr_2$ falls between that of $FeZr_2$ and $NiZr_2$, correlating with a moderate uniaxial NTE and the CTE that also lies between $FeZr_2$ and $NiZr_2$. The predominant vibration modes observed in $NiZr_2$ yield positive γ_c values, which corresponds to a PTE. The observed phenomena indicate that CTE regulation is closely tied to the number of modes with negative γ_c, the more negative modes, the stronger the NTE.

To clarify the quantitative relationship between the Grüneisen parameters and CTEs, the overall $\bar{\gamma}_c$ as a function of the temperature has been computed for the three end point compositions [Fig. 2(b)]. The overall $\bar{\gamma}$ represents the weighted sum of all phonon modes excited at a specific temperature. As the number of M-3d electrons increases, the overall $\bar{\gamma}_c$ steadily increases across the calculated temperature range. Both $FeZr_2$ and $CoZr_2$ have negative overall $\bar{\gamma}_c$ values, with $FeZr_2$ being the most negative and $CoZr_2$ moderately negative. In contrast, $NiZr_2$ consistently shows positive $\bar{\gamma}_c$. It can be noted that the overall $\bar{\gamma}_a$ and $\bar{\gamma}_c$ values tend toward a stable value after 200 K. For a more direct comparison of the overall $\bar{\gamma}$ values, the overall $\bar{\gamma}_a$ and $\bar{\gamma}_c$ at 300 K for the three end point compositions are listed in Fig. 2(c) (detailed γ_a and $\bar{\gamma}_a$ are displayed in Supplemental Material Figs. S11 and S12 [30]). In isotropic materials, the CTE is proportional to the magnitude of γ and has the same sign [52,53]. However, for anisotropic MZr_2, the magnitude of the overall $\bar{\gamma}_c$ at 300 K is -0.98 for $FeZr_2$ with a CTE of -44.63×10^{-6} K^{-1}, while it is 1.47 for $NiZr_2$ with a CTE of $+5.37 \times 10^{-6}$ K^{-1}. Obviously, the CTE magnitude is not quantitatively modeled as directly proportional to $\bar{\gamma}_c$ in the MZr_2 system. This implies that phonons may not be the only factor influencing the wide-range control of CTE in the MZr_2 system.

To further elucidate the determining factors of $\bar{\gamma}_c$, the chemical bond strength was obtained from EXAFS, which helps to uncover the underlying mechanisms of changes in thermal expansion behavior. The crystal structure of MZr_2 is constituted by the corner-shared octahedra of MZr_4 units [28]. The bond-stretching effective force constants ($\kappa_{||}$) for $Zr-M$ and M–M bonds in the MZr_4 octahedra can be acquired through EXAFS, where the $\kappa_{||}$ reflects the strength of the chemical bonds [54] (a detailed data analysis of EXAFS is shown in Supplemental Material Figs. S13–S16 and Tables S1 and S2 [30]). Interestingly, there exists an almost linear correlation between the $\kappa_{||}$ values of $Zr-M$ and M–M bonds and their overall $\bar{\gamma}_c$ values in three end point compositions [Fig. 2(d) and Supplemental Material Fig. S17 [30]]. This direct experimental evidence provides insight into that the weaker bonds more readily generate a negative γ_c, indicating that weaker bonds are more likely to induce NTE along the c axis in the MZr_2 system.

Based on Grüneisen theory, it has been discovered that in anisotropic materials, not only can negative Grüneisen constants induce NTE, but anisotropic elasticity can also excite NTE [18,25]. The axial thermal expansion for the tetragonal MZr_2 is described by [19,25]

TABLE I. Summary of the linear compressibilities for $FeZr_2$, $CoZr_2$, and $NiZr_2$.

χ_a and χ_c(GPa^{-1})	$FeZr_2$	$CoZr_2$	$NiZr_2$
χ_a	0.00245	0.00246	0.00250
χ_c	0.00320	0.00342	0.00332

$$\alpha_a = C_t/V\{\chi_a\gamma_a + S_{13}(\gamma_c - \gamma_a)\}, \quad (1)$$

$$\alpha_c = C_t/V\{\chi_c\gamma_c - 2S_{13}(\gamma_c - \gamma_a)\}, \quad (2)$$

where C_t is the heat capacity at constant stress, and S_{ij} denotes an element of the elastic compliance tensor. The linear compressibilities χ_a and χ_c are given by [25]

$$\chi_a = S_{11} + S_{12} + S_{13}, \quad (3)$$

$$\chi_c = 2S_{13} + S_{33}. \quad (4)$$

Both C_t and V are positive values, indicating that the CTEs (α_a and α_c) are governed by the sign and magnitude of the binomial summation relations between γ_a, γ_c, and S_{ij}. The anisotropic elastic stiffness and elastic compliance tensors for the three end point compositions have been calculated (see Supplemental Material Tables S3 and S4 [30]).

Equations (3) and (4) of the axial CTEs in MZr_2 can be seen as being composed of two parts: a quasicubic term ($\chi_a\gamma_a$ or $\chi_c\gamma_c$) and a cross-linking term $S_{13}(\gamma_c - \gamma_a)$ [25]. Both terms consist of the interaction expressed in a multiplicative form between the phonon-determined axial Grüneisen parameters and the elastic compliances. Here, given the similar crystal structures of different MZr_2 compositions and the small difference in atomic numbers at the M site, V and C_t in Eqs. (1) and (2) for the different compositions are considered approximately equal. According to Eq. (2), the value of α_c can be considered as quantified by the quasicubic term $\chi_c\gamma_c$ and the cross-linking term $S_{13}(\gamma_c - \gamma_a)$. Concerning the quasicubic term, the linear compressibility χ_c remains almost consistent across the three end point compositions (Table I). With the increase in M-3d electrons, taking 300 K as an example, there is a swift transition from negative to positive overall $\bar{\gamma}_c$, causing a dramatic rise in $\chi_c\bar{\gamma}_c$ [Fig. 3(b)]. Hence, the primary contributor to the quasicubic term $\chi_c\bar{\gamma}_c$ in α_c is the overall $\bar{\gamma}_c$ concerning the three end point compositions. For the cross-linking term $-2S_{13}(\bar{\gamma}_c\text{-}\bar{\gamma}_a)$, the difference in axial Grüneisen parameters ($\bar{\gamma}_c\text{-}\bar{\gamma}_a$) increases significantly [Fig. 3(a)], resulting in a sharp decline in its contribution to the c-axis NTE. However, $|S_{13}|$ gradually increases, and considering the sign factor, the cross-linking coefficient S_{13} indicates an enhancement of NTE. Noteworthy, ($\bar{\gamma}_c\text{-}\bar{\gamma}_a$) sharply increases from −4.87 in $FeZr_2$ to −0.47 in $NiZr_2$, rapidly increasing by nearly tenfold, while the cross-linking coefficient $|S_{13}|$ changes from 0.0015 in $FeZr_2$ to 0.0026 in $NiZr_2$, representing an approximate 70% change with relatively minor variation. The interaction between ($\bar{\gamma}_c\text{-}\bar{\gamma}_a$) and $|S_{13}|$ results in the cross-linking term exhibiting a wide-range monotonic increase [Fig. 3(b)]. Evidently, the regulation of CTE by the cross-linking term is primarily dominated by the rapid increase in ($\bar{\gamma}_c\text{-}\bar{\gamma}_a$), which weakens the NTE. Although the value of S_{13} exhibits relatively small variation, it plays a crucial role in enhancing the NTE.

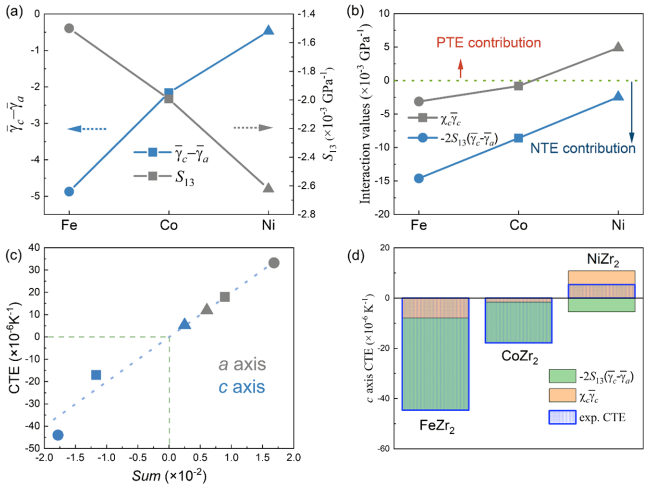

FIG. 3. (a) The $\bar{\gamma}_c\text{-}\bar{\gamma}_a$ and the elastic compliance tensors S_{13} with different numbers of M-3d electrons for MZr_2. (b) Interaction values of the quasicubic and cross-linking terms for MZr_2, where positive values indicate contributions to PTE, and negative values indicate contributions to NTE. (c) Anisotropic CTE versus Sum, where gray and blue represent $\mathrm{Sum}_a[\{\chi_a\gamma_a + S_{13}(\gamma_c - \gamma_a)\}]$ for the a axis and $\mathrm{Sum}_c[\{\chi_c\gamma_c - 2S_{13}(\gamma_c - \gamma_a)\}]$ for the c axis. Symbols (circles, squares, triangles) denote $FeZr_2$, $CoZr_2$, and $NiZr_2$, respectively. (d) Contributions of quasicubic and cross-linking terms to the c-axis CTE, with the blue box showing experimental CTE (average 150–500 K from NPD).

To better quantify the CTEs in the MZr_2 system, Sum_a and Sum_c (collectively referred to as Sum) are used to represent the sum of the quasicubic and cross-linking terms in Eqs. (1) and (2), denoted as $\{\chi_a\gamma_a + S_{13}(\gamma_c\text{-}\gamma_a)\}$ and $\{\chi_c\gamma_c - 2S_{13}(\gamma_c\text{-}\gamma_a)\}$, respectively. Remarkably, in the three end point compositions of MZr_2, there exists an almost linear relationship between the Sum values of the a and c axes and the corresponding CTEs [Fig. 3(c)]. According to Eqs. (1) and (2), when the unit cell parameters and heat capacity changes of the three end point compositions are negligible, the Sum value theoretically exhibits a linear relationship with the M-3d electron count that passes through the origin. The experimental results also show a linear relationship passing through the origin, confirming the consistency between the experimental findings and theoretical calculations. Moreover, quantifying the interaction between phonons and anisotropic elasticity that results in a negligible Sum value implies an insignificant CTE. This offers a good explanation for the axial ZTE observed in

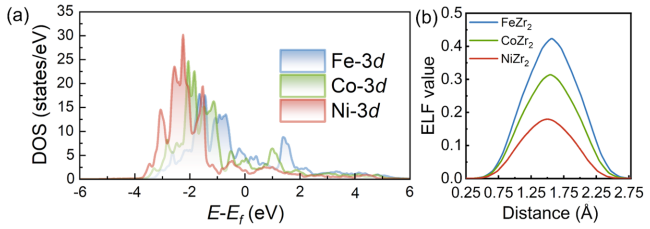

FIG. 4. (a) The most remarkable change in the electronic DOS in M-3d states of the three end point compositions. (b) ELF values for the Zr–Zr bond within the a-b plane with the distance less than 3.2 Å.

$(Co_{0.5}Ni_{0.5})Zr_2$ and $(Fe_{0.2}Ni_{0.8})Zr_2$ (Supplemental Material Fig. S6 [30]) attributed to the negligible Sum of the c axis.

Figure 3(d) visually quantified the contributions from the quasicubic term and the cross-linking term, which are determined by the interaction between phonon-determined Grüneisen parameters and elasticity-determined compliance tensors. It shows that the majority of the NTE along the c axis in $FeZr_2$ and $CoZr_2$ is contributed by the cross-linking term, while the c-axis PTE in $NiZr_2$ is determined by the quasicubic term. Additionally, control over the a-axis thermal expansion is also disclosed (see Supplemental Material Sec. II for details [30]). To conclude, these findings indicate that quantifying the interaction between phonons and elasticity can directly reflect the source of NTE contribution and provide deep insight into the extensive CTE regulation mechanism in the MZr_2 system. This regulatory approach can be applied to other anisotropic thermal expansion systems.

To elucidate the influence of electronic structure on phonons and anisotropic elasticity, with the aim of understanding the broad CTE tunability in MZr_2, density of states (DOS) and electron localization function (ELF) calculations were performed. For the three end point compositions, the projected DOS of M atoms exhibits the most significant changes (Supplemental Material Fig. S18 [30]), notably characterized by a shift toward lower energy regions with an increasing M-3d electron count [Fig. 4(a)]. Variations in M-3d states influence atomic bonding interactions [55,56]. The changes in $Zr-M$ and M–M bonding interactions are also reflected in experimental EXAFS results, which show that Fe–Fe and Zr–Fe are the weakest bonds and confirm that weaker bonds more readily generate negative γ_c [Fig. 2(d)]. Additionally, differences in 3d electron counts result in varying ELF values, with the Zr–Zr bonds (distance < 3.2 Å) in the a-b plane showing the most pronounced discrepancies [Fig. 4(b) and Supplemental Material Figs. S19 and S20 [30]]. Changes in ELF values reflect the evolution of chemical bond properties and lattice mechanical behavior, leading to variations in anisotropic elasticity under different M-3d electronic structures (see Supplemental Material Sec. I for details [30]). Consequently, the changes in bonding interactions induced by M-3d electron count variations dictate the evolution of phonon and elastic properties, making the wide-range CTE tunability in the MZr_2 system possible [30].

In summary, extensive control of CTE has been achieved in the MZr_2 system from 150 to 500 K. The quantified source of NTE in the MZr_2 system is due to the quasicubic and cross-linking terms determined by the interaction between phonons and elasticity. Additionally, the mechanisms for quantitatively regulating CTE over a broad range have been thoroughly elucidated. Combining the temperature dependence of NPD, NPDF, SXRD, and phonon dispersion curves provides deep insights into the lattice dynamics in MZr_2, illustrating that stronger NTE possesses more vibrational modes with negative γ_c. Soft $Zr-M$ and M–M bonds are inclined to lead to a negative overall $\bar{\gamma}_c$, as confirmed by the effective force constants derived from EXAFS. The quantitative roles of phonons and elasticity in the broad regulation of CTE display different effects in MZr_2. As the number of M-3d electrons increases, phonons not only diminish their contribution to NTE in the quasicubic term, but also rapidly decrease in the cross-linking term due to the rapid increase in the axial Grüneisen parameter difference $(\bar{\gamma}_c\text{-}\bar{\gamma}_a)$. Although elasticity changes within the cross-linking term somewhat enhance the NTE, phonon changes play a decisive role in regulating CTE. Moreover, the analysis of the DOS and ELF has disclosed that variations in chemical bonding and elasticity are due to alterations in the electronic structure of M-3d. This Letter offers novel insights for designing high-performance NTE materials and provides guidance for the precise design of CTE.

Acknowledgments—This work was supported by the National Key Research and Development Program of China (Grant No. 2022YFE0109100), the National Natural Science Foundation of China (Grants No. 22235002, No. 22471246, No. 22205016, and No. 22275014), Outstanding Young Scientist Program of Beijing Colleges and Universities (Grant No. JWZQ20240101015), and the China Postdoctoral Science Foundation (Grant No. 2024M750173). This research used resources of the Advanced Photon Source, a U.S. Department of Energy (DOE) Office of Science User Facility operated for the DOE Office of Science by the Argonne National Laboratory under Contract No. DE-AC02-06CH11357. We thank the European Synchrotron Radiation Facility for provision of synchrotron radiation (Exp. No. HC-4185) and all the staff of the BM08-LISA beamline for technical assistance. *In situ* neutron diffraction work was carried out at the NOMAD, Spallation Neutron Source, Oak Ridge National Laboratory. All calculations were supported by the National Supercomputing Center in Zhengzhou.

[1] T. Mary, J. Evans, T. Vogt, and A. Sleight, Science **272**, 90 (1996).
[2] P. Mohn, Nature (London) **400**, 18 (1999).

[3] Y. Zhang, B. Chen, D. Guan, M. Xu, R. Ran, M. Ni, W. Zhou, R. O'Hayre, and Z. Shao, Nature (London) **591**, 246 (2021).
[4] M. T. Dove and H. Fang, Rep. Prog. Phys. **79**, 066503 (2016).
[5] H. Zhou *et al.*, Microstructures **2**, 2022018 (2022).
[6] A. L. Goodwin, M. Calleja, M. J. Conterio, M. T. Dove, J. S. Evans, D. A. Keen, L. Peters, and M. G. Tucker, Science **319**, 794 (2008).
[7] Q. Gao, Y. Jiao, Q. Sun, J. A. Sprenger, M. Finze, A. Sanson, E. Liang, X. Xing, and J. Chen, Angew. Chem., Int. Ed. Engl. **136**, e202401302 (2024).
[8] N. Shi, A. Sanson, Q. Gao, Q. Sun, Y. Ren, Q. Huang, D. O. de Souza, X. Xing, and J. Chen, J. Am. Chem. Soc. **142**, 3088 (2020).
[9] L. Hu *et al.*, J. Am. Chem. Soc. **138**, 14530 (2016).
[10] C. W. Li, X. Tang, J. A. Munoz, J. B. Keith, S. J. Tracy, D. L. Abernathy, and B. Fultz, Phys. Rev. Lett. **107**, 195504 (2011).
[11] B. K. Greve, K. L. Martin, P. L. Lee, P. J. Chupas, K. W. Chapman, and A. P. Wilkinson, J. Am. Chem. Soc. **132**, 15496 (2010).
[12] C. Schneider, D. Bodesheim, M. G. Ehrenreich, V. Crocellà, J. Mink, R. A. Fischer, K. T. Butler, and G. Kieslich, J. Am. Chem. Soc. **141**, 10504 (2019).
[13] D. Dubbeldam, K. S. Walton, D. E. Ellis, and R. Q. Snurr, Angew. Chem., Int. Ed. Engl. **119**, 4580 (2007).
[14] Y. Cao *et al.*, Phys. Rev. Lett. **127**, 055501 (2021).
[15] Y. Song *et al.*, J. Am. Chem. Soc. **140**, 602 (2018).
[16] J. Chen, L. Fan, Y. Ren, Z. Pan, J. Deng, R. Yu, and X. Xing, Phys. Rev. Lett. **110**, 115901 (2013).
[17] M. van Schilfgaarde, I. Abrikosov, and B. Johansson, Nature (London) **400**, 46 (1999).
[18] M. Braden, G. André, S. Nakatsuji, and Y. Maeno, Phys. Rev. B **58**, 847 (1998).
[19] E. T. Ritz and N. A. Benedek, Phys. Rev. Lett. **121**, 255901 (2018).
[20] Y. Qiao *et al.*, npj Quantum Mater. **6**, 49 (2021).
[21] Z. Pan *et al.*, Chem. Mater. **31**, 1296 (2019).
[22] V. Gava, A. L. Martinotto, and C. A. Perottoni, Phys. Rev. Lett. **109**, 195503 (2012).
[23] Y. Oba, T. Tadano, R. Akashi, and S. Tsuneyuki, Phys. Rev. Mater. **3**, 033601 (2019).
[24] Q. Gao *et al.*, Inorg. Chem. **57**, 10918 (2018).
[25] R. Munn, J. Phys. C **5**, 535 (1972).
[26] C. Ablitt, S. Craddock, M. S. Senn, A. A. Mostofi, and N. C. Bristowe, npj Comput. Mater. **3**, 44 (2017).
[27] C. P. Romao, S. P. Donegan, J. Zwanziger, and M. A. White, Phys. Chem. Chem. Phys. **18**, 30652 (2016).
[28] M. Xu *et al.*, Nat. Commun. **14**, 4439 (2023).
[29] Y. Mizuguchi, M. R. Kasem, and Y. Ikeda, J. Phys. Soc. Jpn. **91**, 103601 (2022).
[30] See Supplemental Material at http://link.aps.org/supplemental/10.1103/35ff-84fc for additional discussions and supporting references, which include Refs. [31–47].
[31] F. d'Acapito, G. O. Lepore, A. Puri, A. Laloni, F. La Manna, E. Dettona, A. De Luisa, and A. Martin, J. Synchrotron Radiat. **26**, 551 (2019).
[32] D. C. Koningsberger and R. Prins, *X-ray Absorption: Principles, Applications, Techniques of EXAFS, SEXAFS and XANES* (Wiley, New York, 1987).
[33] A. L. Ankudinov, B. Ravel, J. J. Rehr, and S. D. Conradson, Phys. Rev. B **58**, 7565 (1998).
[34] M. Newville, B. Ravel, D. Haskel, J. Rehr, E. Stern, and Y. Yacoby, Physica (Amsterdam) **208B**, 154 (1995).
[35] G. Kresse and J. Furthmüller, Phys. Rev. B **54**, 11169 (1996).
[36] J. P. Perdew, K. Burke, and M. Ernzerhof, Phys. Rev. Lett. **77**, 3865 (1996).
[37] G. Kresse and D. Joubert, Phys. Rev. B **59**, 1758 (1999).
[38] H. J. Monkhorst and J. D. Pack, Phys. Rev. B **13**, 5188 (1976).
[39] V. Wang, N. Xu, J.-C. Liu, G. Tang, and W.-T. Geng, Comput. Phys. Commun. **267**, 108033 (2021).
[40] K. Parlinski, Z. Q. Li, and Y. Kawazoe, Phys. Rev. Lett. **78**, 4063 (1997).
[41] M. W. Terban and S. J. Billinge, Chem. Rev. **122**, 1208 (2021).
[42] C. Farrow, P. Juhas, J. Liu, D. Bryndin, E. Božin, J. Bloch, T. Proffen, and S. Billinge, J. Phys. Condens. Matter **19**, 335219 (2007).
[43] T. Proffen and S. Billinge, Appl. Crystallogr. **32**, 572 (1999).
[44] E. S. Božin, T. Chatterji, and S. J. L. Billinge, Phys. Rev. B **86**, 094110 (2012).
[45] E. Prince, *Mathematical Techniques in Crystallography and Materials Science* (Springer Science & Business Media, New York, 2012).
[46] A. Savin, R. Nesper, S. Wengert, and T. F. Fässler, Angew. Chem., Int. Ed. Engl. **36**, 1808 (1997).
[47] P. Fuentealba, E. Chamorro, and J. C. Santos, in *Theoretical and Computational Chemistry* (Elsevier, New York, 2007), p. 57.
[48] K. Trueblood, H.-B. Bürgi, H. Burzlaff, J. Dunitz, C. Gramaccioli, H. Schulz, U. Shmueli, and S. Abrahams, Acta Crystallogr. Sect. A **52**, 770 (1996).
[49] S. G. Duyker, V. K. Peterson, G. J. Kearley, A. J. Ramirez-Cuesta, and C. J. Kepert, Angew. Chem., Int. Ed. Engl. **52**, 5266 (2013).
[50] B. T. M. Willis and A. W. Pryor, *Thermal Vibrations in Crystallography* (Cambridge University Press, Cambridge, England, 1975).
[51] H. Bürgi and S. Capelli, Found. Crystallogr. **56**, 403 (2000).
[52] E. Liang, Q. Sun, H. Yuan, J. Wang, G. Zeng, and Q. Gao, Front. Phys. **16**, 53302 (2021).
[53] J. Chen, L. Hu, J. Deng, and X. Xing, Chem. Soc. Rev. **44**, 3522 (2015).
[54] A. Sanson, Microstructures **1**, 2021004 (2021).
[55] K.-J. Xu *et al.*, Nat. Phys. **19**, 1834 (2023).
[56] C. Broyles, Z. Rehfuss, H. Siddiquee, J. A. Zhu, K. Zheng, M. Nikolo, D. Graf, J. Singleton, and S. Ran, Phys. Rev. Lett. **131**, 036501 (2023).